

Bonding Heterogeneity in Mixed-Anion Compounds Realizes Ultralow Lattice Thermal Conductivity

Naoki Sato, Norihide Kuroda, Shun Nakamura, Yukari Katsura, Ikuzo Kanazawa, Kaoru Kimura, and Takao Mori*

Dr. N. Sato

International Center for Young Scientists (ICYS), National Institute for Materials Science (NIMS)

1-2-1 Sengen, Tsukuba, Ibaraki 305-0047, Japan

E-mail: SATO.Naoki@nims.go.jp.

Dr. N. Sato, Prof. Dr. T. Mori

International Center for Materials Nanoarchitectonics (WPI-MANA), NIMS

1-1 Namiki, Tsukuba, Ibaraki 305-0047, Japan

Mr. N. Kuroda, Mr. S. Nakamura, Prof. Dr. I. Kanazawa

Department of Physics, Tokyo Gakugei University

4-1-1 Nukuikitamachi, Koganei, Tokyo 184-8501, Japan

Dr. Y. Katsura

Research and Services Division of Materials Data and Integrated System (MaDIS), NIMS

1-1 Namiki, Tsukuba, Ibaraki 305-0047, Japan

Prof. Dr. K. Kimura, Dr. Y. Katsura

Department of Advanced Materials Science, The University of Tokyo

5-1-5 Kashiwanoha, Kashiwa, Chiba 277-8561, Japan

Prof. Dr. K. Kimura

OPERANDO-OIL, National Institute of Advanced Industrial Science and Technology (AIST)

5-1-5 Kashiwanoha, Kashiwa, Chiba 277-8561, Japan

Prof. Dr. T. Mori

Graduate School of Pure and Applied Science, University of Tsukuba

1-1-1 Tennodai, Tsukuba, Ibaraki 305-8671, Japan

Keywords: ab initio calculation, bonding heterogeneity, lattice dynamics, lattice thermal conductivity, mixed-anion compound

Crystalline materials with intrinsically low lattice thermal conductivity (κ_{lat}) pave the way towards high performance in various energy applications, including thermoelectrics. Here we demonstrate a strategy to realize ultralow κ_{lat} using mixed-anion compounds. Our calculations reveal that locally distorted structures in chalcogenides MnPnS_2Cl ($\text{Pn} = \text{Sb, Bi}$) derives a bonding heterogeneity, which in turn causes a peak splitting of the phonon density of states. This splitting induces a large amount of scattering phase space. Consequently, κ_{lat} of MnPnS_2Cl

is significantly lower than that of a single-anion sulfide CuTaS_3 with a similar crystal structure. Experimental κ_{lat} of MnPnS_2Cl takes an ultralow value of about $0.5 \text{ W m}^{-1} \text{ K}^{-1}$ at 300 K. Our findings will encourage the exploration of thermal transport in mixed-anion compounds, which remain a vast unexplored space, especially regarding unexpectedly low κ_{lat} in lightweight materials derived from the bonding heterogeneity.

1. Introduction

Searches for low lattice thermal conductivity (κ_{lat}) materials have been of great importance in achieving high performance in thermoelectrics,^[1–3] thermal barrier coatings,^[4] and thermal insulation.^[5] In the past decade, the validity of some extrinsic effects for reducing κ_{lat} , such as point defects,^[6,7] fine grain boundary,^[8] nanoscale precipitates,^[9] and all-scale hierarchical microstructures,^[10] has been successfully demonstrated. However, these strategies usually affect charge carrier mobility, which is detrimental to thermoelectric performance. Thus, understanding the intrinsic mechanisms of thermal transport realizing low κ_{lat} which are associated closely with chemical bonding, crystal structure, and lattice anharmonicity, can be more helpful in some cases, as it provides us with efficient ways to manage both electrical and thermal properties independently.

In recent years, several structural origins bringing intrinsically low κ_{lat} like complex crystal structure,^[11–20] resonant bonding,^[21–23] stereochemically active lone-pair electrons,^[24–31] rattling and its reminiscent anharmonic vibration,^[30,32–42] superionic transition,^[43–47] partial occupancy,^[48,49] and bonding heterogeneity^[27,40,50–56] have been unveiled. Among these, we focus on the bonding heterogeneity, namely the coexistence of strong and weak bonding, as it is more likely to be observed in many classes of crystalline solids and can be utilized more easily to realize low κ_{lat} . The bonding heterogeneity is frequently observed in Zintl phases, which consist of coexisting ionic and covalent sublattices. In addition, local structures

containing multiple anions should form a distorted coordination environment, which gives the bonding heterogeneity.

Mixed-anion compounds, solid-state materials containing more than one anionic species in a single phase, have recently attracted much attention because they have potential to offer novel and attractive functionalities which were not observed in conventional “single-anion” materials.^[57] Some superior properties in the mixed-anion compounds have already been discovered, such as visible-light photocatalysis, pleochroism, and battery applications.^[57] In the thermoelectrics field, anionic solid solutions like PbTe–PbSe^[58,59] and Bi₂Te₃–Bi₂Se₃^[60] have been regarded as an effective way to realize carrier concentration tuning, band engineering, and reduction of κ_{lat} via phonon-alloy scattering. In addition, a mixed-anion BiCuSeO consisting of (Cu₂Se₂)²⁻ and (Bi₂O₂)²⁻ layers has been a hot material because of its extremely low κ_{lat} and promising figure of merit.^[61–63] The origin of low κ_{lat} is derived from large anharmonicity due to the anisotropic layered structure. It is a typical example of mixed-anion compounds containing multiple anions in separate building blocks. On the other hand, the mixed-anion are also likely to form locally distorted structures in which more than one anions are bonded to a cation. This class of materials is less explored in terms of thermal transport. Although a few previous reports^[51–53] deal with this type mixed-anion materials, unique features derived from the mixed-anions are still ambiguous because they are not compared with a single-anion counterpart. We can expect that the locally distorted structures in mixed-anion materials bring the bonding heterogeneity, which effectively realize low κ_{lat} .

Herein, we demonstrate an effective guideline that the mixed-anion framework with distorted local structures is a promising series of materials to realize ultralow κ_{lat} . We chose Mn-based chalcogenides MnPnS₂Cl (Pn = Sb, Bi) as model materials to test the validity of our strategy using mixed-anion compounds. To extract unique features derived from the mixed-anion, a single-anion sulfide CuTaS₃, which has some structural similarities to the mixed-anion chalcogenides, was chosen for comparison. By performing calculations based on density

functional theory (DFT), we explore lattice dynamics and thermal transport properties of these compounds. We find a remarkable variety of second order interatomic force constants (IFC) within the distorted coordination polyhedra containing multiple anions, which shows significant bonding heterogeneity in this series. Some peak-splitting in the phonon density of states (DOS) originating from the bonding heterogeneity significantly increases the 3-phonon scattering phase space (SPS), which results in a much smaller phonon relaxation time of MnPnS_2Cl than CuTaS_3 . Consequently, the calculated κ_{lat} of MnPnS_2Cl is strikingly about seven times lower than CuTaS_3 . The synthesized polycrystalline sample of MnPnS_2Cl is actually demonstrated to exhibit the ultralow κ_{lat} of about $0.5 \text{ W m}^{-1} \text{ K}^{-1}$ at room temperature. Considering the relatively low density and averaged atomic mass of MnSbS_2Cl , this mixed-anion approach can give a route to uncover lightweight materials with low κ_{lat} .

2. Results and Discussion

The crystal structures of mixed-anion chalcogenides MnPnCh_2X ($\text{Pn} = \text{Sb, Bi, Ch} = \text{S, Se, X} = \text{Cl, Br, I}$) series, including our target materials, were originally investigated by single-crystal X-ray and neutron diffraction.^[64–66] Figure 1a shows the crystal structure of the mixed-anion chalcogenides visualized by VESTA 3.^[67] MnSbS_2Cl and MnBiS_2Cl crystallize in the orthorhombic structure (space group $Pnma$).^[64,65] The primitive cell contains five crystallographically inequivalent atoms, Mn, Sb/Bi, S(1), S(2), and Cl. All the atoms occupy 4c Wyckoff position. These compounds are composed of locally distorted structures derived from constituent multiple anions. The coordination environments around Mn and Sb/Bi atoms are shown in Figures 1b and 1c, respectively. The Mn atom is octahedrally coordinated by four S and two Cl atoms with *cis*-geometry. The Sb/Bi atom is coordinated by five S and three Cl atoms. The interatomic distances between Sb/Bi and Cl are much longer than those between Sb/Bi and S atoms. These polyhedra share their edges and vertices and form infinite chains along the *b*-axis. The locally distorted structures containing different bond lengths and chemical

environments should result in a significant bonding heterogeneity, which in turn can cause interesting lattice dynamics and thermal transport properties.

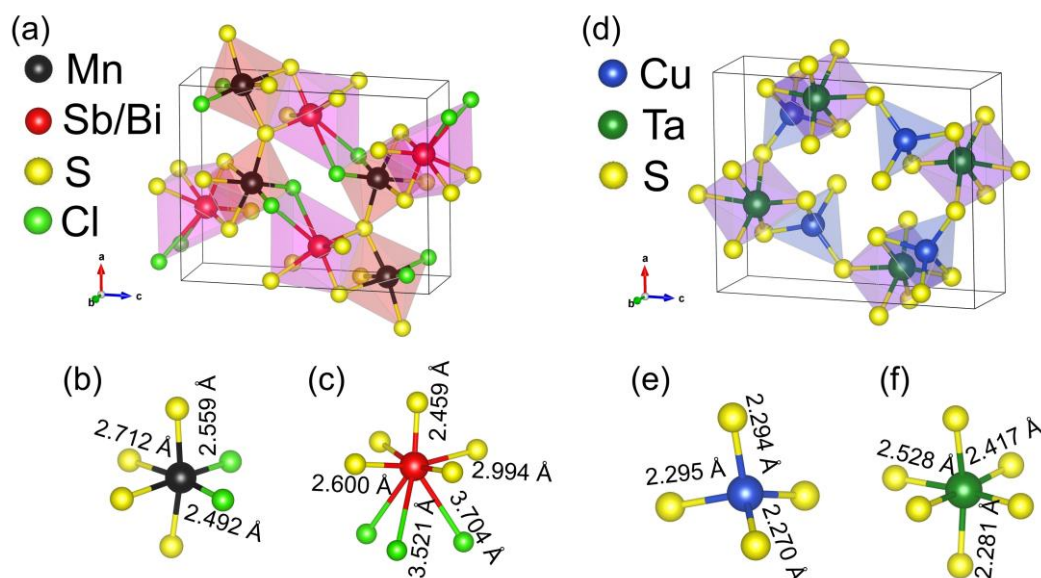


Figure 1. a) The unit cells of MnPnS_2Cl ($\text{Pn} = \text{Sb}, \text{Bi}$) and the coordination environments around b) Mn and c) Sb/Bi atoms. d) The unit cell of CuTaS_3 and the coordination environment around e) Cu and f) Ta atoms. The interatomic distances of atom pairs are shown along each bond. The value shown in b) and c) correspond to MnSbS_2Cl .

It is necessary to make a comparison between the mixed-anion compounds and a single-anion counterpart which resembles each other, in order to extract unique features originating from the mixed-anion state. CuTaS_3 , a single-anion sulfide, has some structural similarity to MnPnS_2Cl . Figure 1d shows the crystal structure of CuTaS_3 . CuTaS_3 crystallizes in the orthorhombic structure with space group $Pnma$, and the primitive cell contains five crystallographically inequivalent atoms, Cu, Ta, S(1), S(2), and S(3).^[68] All the atoms occupy 4c Wyckoff position. The coordination environments around Cu and Ta atoms are shown in Figures 1e and 1f, respectively. In the ICSD database, MnPnCh_2X is classified as the same structure-type as CuTaS_3 though the local structures are quite different. The Cu atom is tetrahedrally coordinated by three S atoms, and the Ta atom is octahedrally coordinated by six S atoms. The bond lengths within the coordination polyhedra vary despite the single anion, but to a lesser extent than the mixed-anion MnPnS_2Cl . In addition, MnBiS_2Cl and CuTaS_3 have the

similar theoretical density of 5.32 g cm^{-3} and 5.82 g cm^{-3} , respectively, and the same percentage of heavy atoms where 20% of the constituent elements are heavy (Sb, Bi, Ta) and 80% are relatively light (Mn, Cu, S, Cl). Thus, CuTaS_3 is a suitable material to compare the lattice dynamics with MnPnS_2Cl to gain insight into the crucial roles of the mixed-anion.

We performed DFT-based calculations (see Computational Method in the Supporting Information) to investigate lattice dynamics and thermal transport properties of the mixed-anion MnPnS_2Cl and the single-anion CuTaS_3 . Figure 2 shows the norm of calculated second-order IFC matrix, $|\Phi^{ij}|$ as a function of interatomic distance. The IFC represents the strength of interaction between each atomic pair, namely bond strength. The IFCs decay rapidly with increasing interatomic distance though some non-negligible components are observed for Sb-S, Bi-S, and Ta-S bonds at around 6 Å. The IFCs of Cu-S bonds in the coordination tetrahedron of CuTaS_3 with almost identical bond length range from 4 to 5 eV Å^{-2} , while those of Ta-S bonds range from 4 to 7 eV Å^{-2} due to slightly different bond length and distorted coordination. On the other hand, the IFCs of the nearest and second nearest Mn-S and Mn-Cl differ by a factor of about 3–6. For the nearest Sb-S (Bi-S) and Sb-Cl (Bi-Cl), the IFCs differ by a factor of 23 (18). These indicate that the local structures in the mixed-anion MnPnS_2Cl hold the remarkable bonding heterogeneity compared to CuTaS_3 . This significant difference of bonding environment between the mixed- and single-anion compounds can cause interesting features in lattice dynamics.

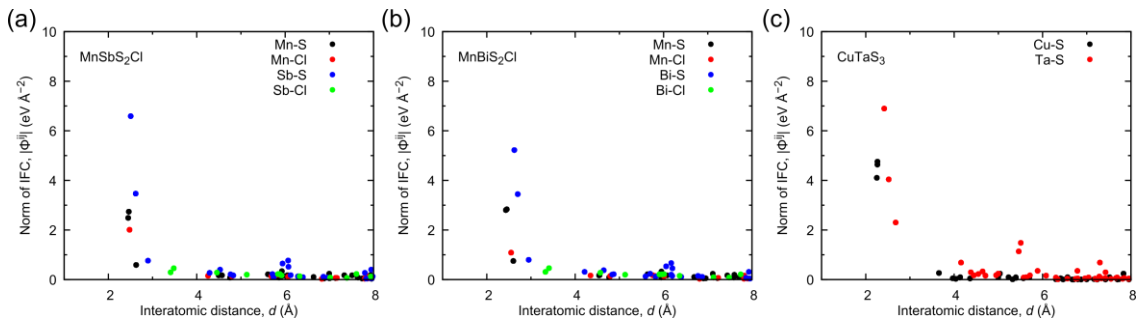


Figure 2. Norm of IFC matrix, $|\Phi^{ij}|$, as a function of interatomic distance between atoms denoted by i and j for a) MnSbS_2Cl , b) MnBiS_2Cl , and c) CuTaS_3 .

The calculated phonon dispersion curves together with the phonon DOS are shown in Figures 3a, 3b, and 3c. These compounds are dynamically stable as no imaginary modes are observed in the phonon dispersion. As shown in the atom-decomposed phonon DOS, the acoustic modes mainly originate from the heaviest atom (Sb, Bi, and Ta for MnSbS₂Cl, MnBiS₂Cl, and CuTaS₃, respectively). For CuTaS₃, high-frequency optical modes ($> 250 \text{ cm}^{-1}$) mainly derive from S atom, while heavier Cu and Ta atoms mainly contribute to the lower modes ($< 180 \text{ cm}^{-1}$). As a result, a gap-like opened structure is observed in the phonon DOS at around $180\text{--}250 \text{ cm}^{-1}$. On the other hand, the gap-like structure is not observed in the phonon DOS of MnPnS₂Cl. For MnPnS₂Cl, high-frequency region ($> 200 \text{ cm}^{-1}$) is like CuTaS₃, namely large contribution from S atom. However, Cl atom contributes to the lower frequency region ($70\text{--}200 \text{ cm}^{-1}$) despite its almost the same atomic mass as S (S: 32.07 g mol^{-1} , Cl: 35.45 g mol^{-1}). This splitting of the peak in the phonon DOS between S and Cl is derived from the bonding heterogeneity. The phonon frequency ω is related to the atomic mass and the second-order IFC:

$$\omega^2 \propto \frac{1}{\sqrt{M_A M_B}} \sum \Phi \quad (1)$$

where M_A and M_B are the atomic mass of species A and B, respectively, and Φ is the second-order IFC. Thus, a significant variety of the IFC originating from the bonding heterogeneity results in the splitting of phonon frequency, even though the atomic mass of multiple anions is almost the same. Figure 3d shows a schematic diagram representing the situation occurred here. The gap-like structure observed in the phonon DOS of the single-anion material is filled with additional states generated from the peak splitting induced by the bonding heterogeneity in the mixed-anion material with locally distorted structures.

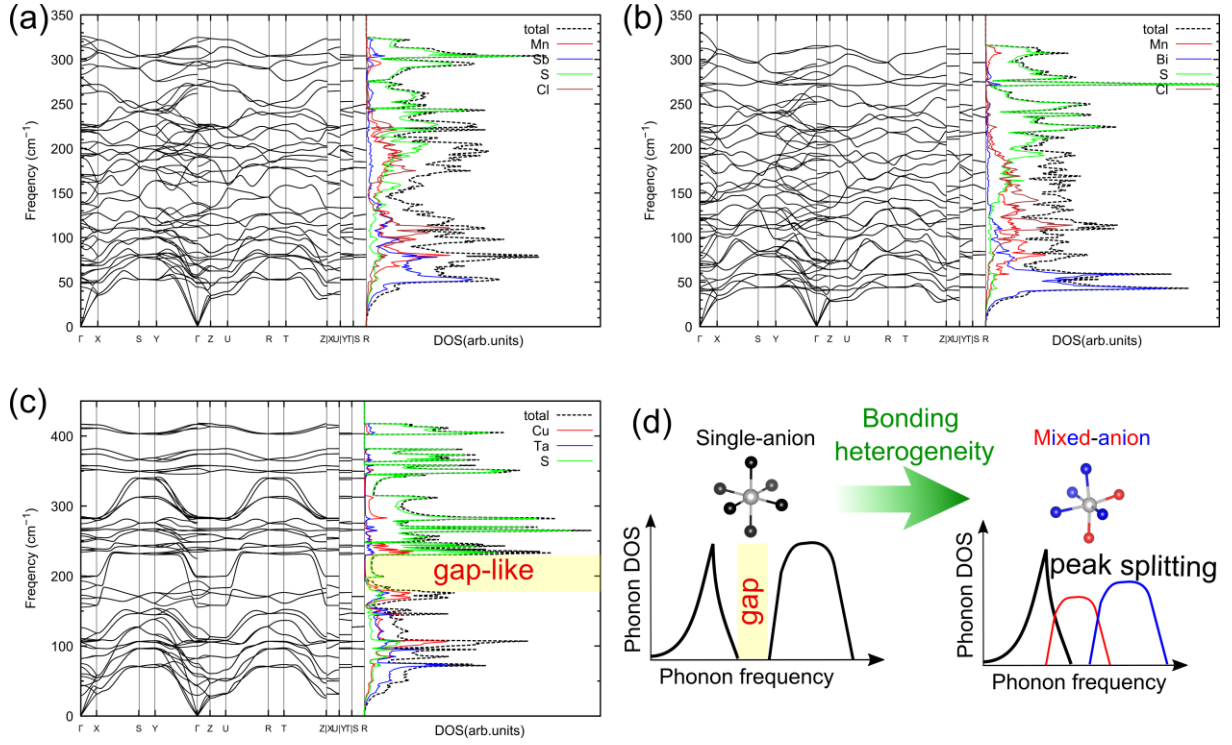


Figure 3. The calculated phonon dispersion and the total and atom-decomposed phonon DOS for a) MnSbS_2Cl , b) MnBiS_2Cl , and c) CuTaS_3 . A colored region in c) represents a gap-like opened structure observed in the phonon DOS of CuTaS_3 . d) A schematic diagram representing the change of phonon DOS from single-anion to mixed-anion materials induced by the bonding heterogeneity. The gap-like structure of DOS observed in the single-anion is filled with additional states formed by peak splitting in the mixed-anion one.

A potential energy surface that provides us with insight into anharmonicity at each atomic site can be visualized by plotting an energy change with respect to a displacement of the atom. Figures 4a, 4b, and 4c show the potential energy of anion sites as a function of displacements along cartesian x -, y -, and z -directions for MnSbS_2Cl , MnBiS_2Cl , and CuTaS_3 , respectively. The potential energy of all sites, including cation sites, is shown in Figure S1 in the Supporting Information. The potential energy exhibits slightly asymmetric features and deviates from parabolic behavior, which shows the high anharmonicity of these compounds. The Cl atoms of MnSbS_2Cl lie in a flatter potential than the S atoms, which is consistent with the weaker bonding environment and the lower phonon frequency of the Cl atoms. The shallow potential well also corresponds to the large thermal displacement parameters represented by the mean square displacement, as shown in Figure S2 in the Supporting Information. To further gain insight into

the anharmonicity of these compounds, we calculated the Grüneisen parameters as shown in Figure 4d. The Grüneisen parameter is defined by the change of phonon frequency with respect to the change of volume of the unit cell. Some compounds possessing lone-pair electrons and low κ_{lat} show anomalously large Grüneisen parameter exceeding 50.^[24,27] For the low frequency region of acoustic modes, the magnitude of the Grüneisen parameter is larger for CuTaS₃ than MnPnS₂Cl while MnPnS₂Cl has larger values at around 50 cm⁻¹ and 150 cm⁻¹. From the Grüneisen parameter, we can see that both MnPnS₂Cl and CuTaS₃ has moderate anharmonicity compared to extremely anharmonic materials.^[24,27]

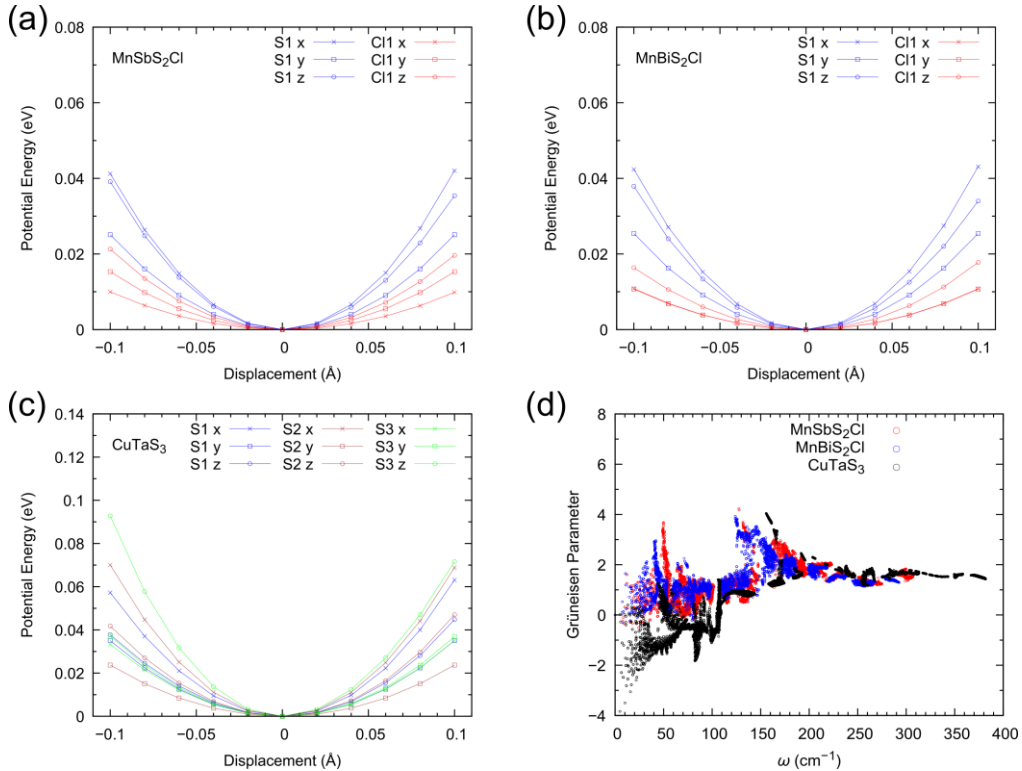


Figure 4. The calculated potential energy of each atomic site as a function of displacements along cartesian x -, y -, and z -directions for a) MnSbS₂Cl, b) MnBiS₂Cl, and c) CuTaS₃. d) The calculated Grüneisen parameter as a function of the phonon frequency.

To achieve further insight into the relationship between the bonding heterogeneity and the thermal transport, we calculated the 3-phonon SPS. The SPS is a measure of the amount of available scattering processes satisfying the energy and momentum conservation. The SPS is given as

$$W_q^\pm = \frac{1}{N} \sum_{q', q''} \left\{ \frac{n_{q''} - n_{q'}}{n_{q'} + n_{q''} + 1} \right\} \delta(\omega_q - \omega_{q'} \pm \omega_{q''}) \quad (2)$$

where W_q^+ and W_q^- are the SPS corresponding to absorption and emission processes of phonon mode q , respectively. Here, the variable q is defined by $q = (\mathbf{q}, j)$ and $-q = (-\mathbf{q}, j)$ where \mathbf{q} and j are the wave vector and the branch index of phonon modes. n_q is the Bose-Einstein distribution function. Figures 5a and 5b show W_q^+ and W_q^- as a function of the phonon frequency at 300 K, respectively. Notably, W_q^+ at the low-frequency region and W_q^- at the middle and high-frequency region are several times larger for MnPnS₂Cl than CuTaS₃. These differences should originate from the peak splitting of phonon DOS discussed above, as represented by Figure 3d. The gap-like structure observed in the phonon DOS causes the lower amount of 3-phonon scattering processes between acoustic-optical and optical-optical modes. The gap is filled with the additional states induced by the bonding heterogeneity, which results in the increase of acoustic-optical and optical-optical scattering processes. The SPS is proportional to the 3-phonon scattering rate, the inverse of phonon relaxation time τ . In other words, the larger the SPS, the smaller the τ . Thus, the larger SPS brings the lower κ_{lat} . Figure 5c shows the 3-phonon relaxation time as a function of the phonon frequency at 300 K. At the overall frequency range, the τ of MnPnS₂Cl is significantly smaller than that of CuTaS₃. As shown in Figure S3 in the Supporting Information, the phonon group velocity of acoustic modes of MnPnS₂Cl and CuTaS₃ is not essentially different, while the optical modes of CuTaS₃ at around 150–250 cm⁻¹, corresponding to the dispersive curve in Figure 3c, have much larger value. However, this large group velocity of the optical modes of CuTaS₃ has a negligible contribution to the lattice thermal conductivity, as shown in the spectral thermal conductivity (Figure S4, Supporting Information). Therefore, the significant difference in the τ between MnPnS₂Cl and CuTaS₃ is a dominant factor determining the difference in κ_{lat} .

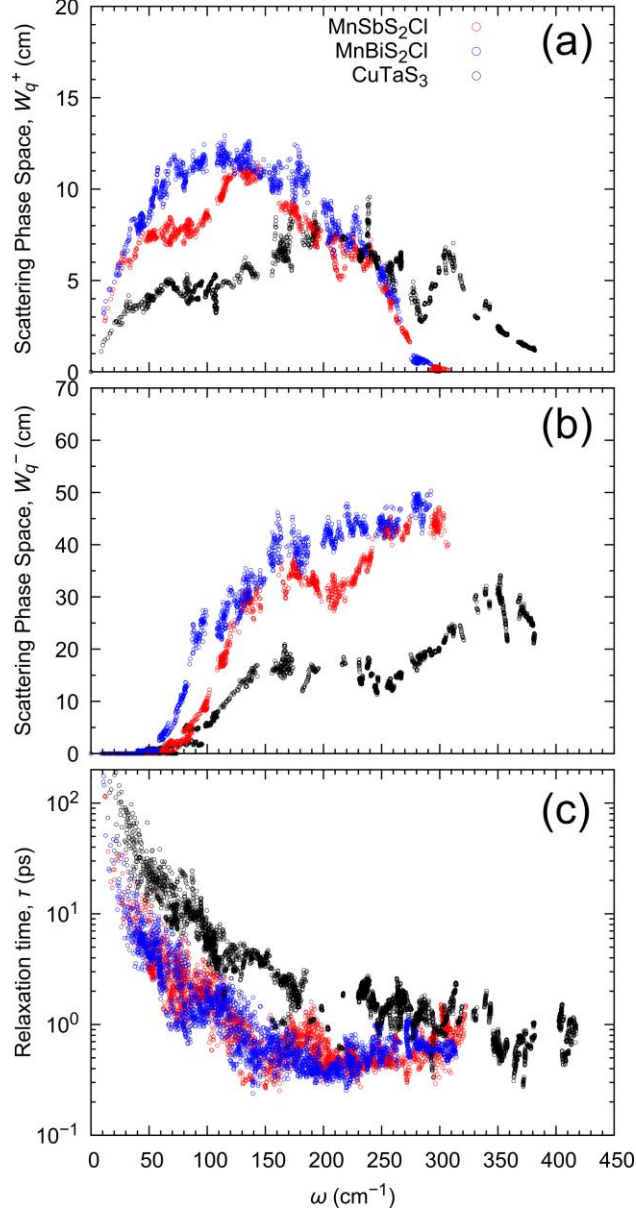


Figure 5. The calculated 3-phonon SPS for a) absorption and b) emission processes, and c) 3-phonon relaxation time at 300 K as a function of the phonon frequency.

We calculated the κ_{lat} by solving the phonon Boltzmann transport equation within the single mode relaxation time approximation. The calculation only considers the intrinsic 3-phonon scattering. Figures 6a, 6b, and 6c show the temperature dependence of the κ_{lat} (xx , yy , and zz components) for MnSbS₂Cl, MnBiS₂Cl, and CuTaS₃, respectively. The averaged value of each direction is also shown. In addition, we synthesized the polycrystalline samples of MnSbS₂Cl, MnBiS₂Cl, and CuTaS₃ by solid-state reaction, melting, and spark plasma sintering and measured the experimental κ_{lat} (see Experimental Procedure and measured X-ray diffraction

patterns in Figure S5 in the Supporting Information). The temperature dependence of the experimental κ_{lat} is plotted in Figures 6a, 6b, and 6c. The calculated κ_{lat} shows a significant anisotropy for these compounds due to the anisotropic crystal structures. The averaged calculated values at 300 K are $1.1 \text{ W m}^{-1} \text{ K}^{-1}$, $1.0 \text{ W m}^{-1} \text{ K}^{-1}$, and $7.2 \text{ W m}^{-1} \text{ K}^{-1}$ for MnSbS_2Cl , MnBiS_2Cl , and CuTaS_3 , respectively. The temperature dependence of the experimental κ_{lat} for MnPnS_2Cl is flat, while the calculated one obeys T^{-1} dependence. The experimental values at 300 K are $0.50 \text{ W m}^{-1} \text{ K}^{-1}$, $0.53 \text{ W m}^{-1} \text{ K}^{-1}$, and $3.5 \text{ W m}^{-1} \text{ K}^{-1}$, respectively. Both the calculated and experimental values differ strikingly by a factor of 7 between MnPnS_2Cl and CuTaS_3 . The deviation between the absolute values of calculated and experimental κ_{lat} can be due to several factors: the experimental κ_{lat} contains the effect of grain boundary and chemical disorder. Moreover, some effects unveiled in recent years are beyond the scope of our calculations, such as the temperature dependent anharmonicity^[69] and crystal/amorphous boundary behavior,^[70,71] which might contribute to the glass-like flat temperature dependence.

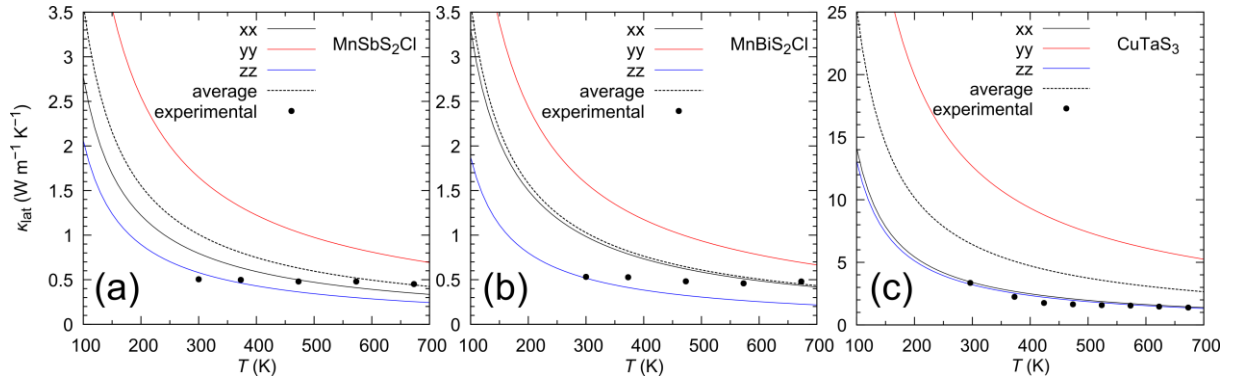


Figure 6. The temperature dependence of calculated and experimental κ_{lat} for a) MnSbS_2Cl , b) MnBiS_2Cl , and c) CuTaS_3 .

We have discovered that the mixed-anion MnPnS_2Cl exhibits the ultralow κ_{lat} even at room temperature. Considering the relatively low density (MnSbS_2Cl : 4.12 g cm^{-3} , MnBiS_2Cl : 5.32 g cm^{-3}) and averaged atomic mass per atom (MnSbS_2Cl : $55.27 \text{ g mol}^{-1} \text{ atom}^{-1}$, MnBiS_2Cl : $72.71 \text{ g mol}^{-1} \text{ atom}^{-1}$), the κ_{lat} values of these compounds are unexpectedly low. Light atoms generally make stronger and more covalent bonding than heavier ones, which typically leads to

high κ_{lat} . To highlight the anomaly of the mixed-anion compounds, we plotted the κ_{lat} versus the averaged atomic mass of various materials, including simple semiconductors and some known thermoelectric materials with low κ_{lat} in Figure 7. Almost all materials with $\kappa_{\text{lat}} < 1 \text{ W m}^{-1} \text{ K}^{-1}$ shown here have large averaged atomic mass larger than $80 \text{ g mol}^{-1} \text{ atom}^{-1}$, except for MnPnS_2Cl , Cu_2S ,^[47] and Cu_4TiSe_4 .^[72] Cu_2S undergoes two phase transitions and possesses liquid-like copper ions, which results in ultralow κ_{lat} .^[47] The extremely low κ_{lat} of Cu_4TiSe_4 , $0.19 \text{ W m}^{-1} \text{ K}^{-1}$ at 300 K, was very recently confirmed and attributed to its highly disordered structure and soft phonon modes.^[72] Note that the lightweight and ultralow κ_{lat} MnPnS_2Cl contains none of the phase transitions, structural instability, and extremely high anharmonicity but contains the bonding heterogeneity induced by the locally distorted structures.

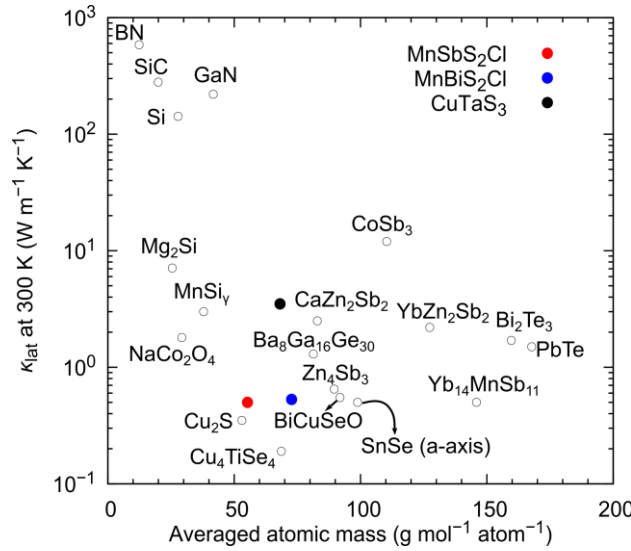


Figure 6. κ_{lat} at 300 K versus averaged atomic mass for various compounds including the mixed-anion MnPnS_2Cl (this work), CuTaS_3 (this work), h-BN (in-plane),^[73] 4H-SiC,^[74] Si,^[75] GaN,^[76] Mg_2Si ,^[77] CoSb_3 ,^[78] Bi_2Te_3 ,^[79] PbTe ,^[80] $\text{Yb}_{14}\text{MnSb}_{11}$,^[81] YbZn_2Sb_2 ,^[81] CaZn_2Sb_2 ,^[81] Zn_4Sb_3 ,^[82] MnSi_7 ,^[14] Cu_2S ,^[47] $\text{Ba}_8\text{Ga}_{16}\text{Ge}_{30}$,^[36] BiCuSeO ,^[61] SnSe (*a*-axis),^[83] NaCo_2O_4 ,^[84] and Cu_4TiSe_4 .^[72]

A great advantage of the bonding heterogeneity by mixed-anion concept to realize low κ_{lat} , summarized in Figure 3d, is that the phonon frequency of light atoms, like Cl in this work, can be lowered so that the number of optical modes whose frequency are close to acoustic modes increases. It means that the strategy can be utilized to explore lightweight and low κ_{lat} materials.

In particular, abundant mixed-anion materials unknown in terms of thermal conductivity, such as oxynitrides, oxysulfides, and chalcogenides, can be promising candidates.

3. Conclusion

In conclusion, we have demonstrated that the locally distorted structures observed in the mixed-anion compounds derive ultralow κ_{lat} . Using DFT-based calculations, we clarified the significant variety of the second-order IFC in the mixed-anion MnPnS_2Cl , which represents the bonding heterogeneity. This bonding environment causes the remarkable splitting of the phonon frequency, which essentially increases the amount of 3-phonon scattering processes. The increased SPS leads to the lower phonon relaxation time. Consequently, κ_{lat} of MnPnS_2Cl is significantly lower than that of a single-anion sulfide CuTaS_3 with the similar crystal structure and percentage of heavy atoms. Experimental κ_{lat} of MnPnS_2Cl shows an ultralow value of about $0.5 \text{ W m}^{-1} \text{ K}^{-1}$ at room temperature, which is unexpectedly low considering the relatively low averaged atomic mass per atom of these compounds. A possible future work will be to confirm whether the strategy found in this work can be applied to a broader range of the mixed-anion compounds. Our study decorates the mixed-anion compounds, which remain a vast unexplored space, with novel thermal functionality.

4. Experimental Section

Synthesis: Polycrystalline samples of MnPnS_2Cl were synthesized by solid state reaction of stoichiometric amounts of MnS , MnCl_2 , and Pn_2S_3 (1:1:1). The starting materials were weighed and ground with an agate mortar in an Ar-filled glovebox, and then transferred to quartz tubes and sealed under a high vacuum. These ampoules were put into a box furnace and heated to 773 K for 2 hours, and kept for 7 days. The obtained ingots were ground into fine powders ($< 45 \mu\text{m}$) and consolidated by spark plasma sintering (SPS, SPS-515S, Fuji Electronic Industrial Co., Japan). To obtain dense and high-purity bulk samples, we applied high-pressure and low-temperature conditions for SPS. The powder samples were set in a 10 mm diameter cemented

carbide die, heated to 813 K with a uniaxial pressure of 500 MPa under Ar atmosphere, and then held for 30 min. The dense bulk samples with relative density ~98% were obtained.

A polycrystalline sample of CuTaS_3 was synthesized by melting and following solid state reaction of element powders Cu, Ta, and S. To avoid S-poor impurity phases, the nominal composition was set to $\text{CuTaS}_{3.2}$. The starting materials were weighed and ground with the agate mortar, and then transferred to a quartz tube and sealed under a high vacuum. The ampoule was put into the box furnace and heated to 923 K for 24 hours, and kept for 7 days. The obtained ingot was ground into fine powders ($< 45 \mu\text{m}$) and consolidated by SPS. The powder sample was set in a 10 mm diameter graphite die, heated to 873 K with a uniaxial pressure of 100 MPa under Ar atmosphere, and then held for 10 min. The dense bulk sample with relative density ~98% was obtained.

Characterization: The phase identification of the samples was performed by X-ray diffraction (XRD) measurements using $\text{Cu K}\alpha$ radiation (SmartLab, Rigaku Co., Japan). The thermal conductivity κ was brought by $\kappa = DC_p d$, where D , C_p , and d are the thermal diffusivity, the specific heat, and the density, respectively. The thermal diffusivity and the specific heat were concurrently measured for the disk-shaped samples by laser flash method (LFA 467 Hyperflash, Netzsch, Germany) with a pyroceram disk as a reference sample. The sample density was measured by Archimedes method. The lattice thermal conductivity κ_{lat} can be regarded as the same as the measured κ because MnPnS_2Cl and CuTaS_3 are insulators with high electrical resistivity.

Computational Method: We performed *ab initio* calculations based on density functional theory (DFT). The Quantum Espresso (QE) package^[85,86] with projector-augmented wave pseudopotentials^[87,88] was used for total energy calculations. The generalized gradient approximation functional with Perdew–Burke–Ernzerhof parametrization revised for solids (GGA-PBEsol)^[89] was employed for the exchange and correlation potentials. For MnPnS_2Cl (Pn = Sb, Bi), we employed spin-polarized settings with oppositely oriented magnetic moments

on Mn atoms. Initial values of magnetic moments of Mn atoms were set to $\pm 5 \mu_B$, and after structure relaxation, they were converged to $\pm 4.19 \mu_B$ and $\pm 4.15 \mu_B$ for MnSbS_2Cl and MnBiS_2Cl , respectively. k -point grids of $6 \times 14 \times 4$ and $6 \times 15 \times 4$ and energy cutoff of 100 Ry and 90 Ry for the primitive cell of MnPnS_2Cl and CuTaS_3 , respectively, were used for structure relaxation. The lattice parameters of the relaxed primitive cell of MnPnS_2Cl and CuTaS_3 are listed in Table S1.

To extract the second and third order interatomic force constants (IFC), we used finite difference method with $2 \times 3 \times 1$ supercells containing 120 atoms based on the fully relaxed primitive cell to create displacement-force datasets. The magnitude of atomic displacements was set at 0.01 Å and 0.04 Å for calculating the second and third order IFCs, respectively. For the third order IFC calculation, we chose the cutoff radius as 14.2 Å for choosing triplets within which interaction is considered. The IFCs were obtained using ALAMODE^[90] code. The phonon dispersion relation and density of states (DOS) were calculated from the second order IFC. The sampling grids used for summation were $7 \times 17 \times 5$ and $7 \times 18 \times 6$ for MnPnS_2Cl and CuTaS_3 , respectively. Dielectric constant and Born effective charge were calculated in the perturbation framework implemented in the QE package for correcting phonon frequencies considering long-range interaction. ALAMODE code is also used to calculate the lattice thermal conductivity by solving the phonon Boltzmann transport equation within the single mode relaxation time approximation. The sampling grids $7 \times 17 \times 5$ and $7 \times 18 \times 6$ for MnSbS_2Cl and MnBiS_2Cl , respectively, were applied after confirming convergence of the calculated lattice thermal conductivity with respect to the grid density.

Acknowledgements

This work was supported by the JSPS JP16H06441, JP17H02749, and JST Mirai Program JPMJMI19A1, CREST JPMJCR19Q4. The computation in this work has been performed using the Numerical Materials Simulator at NIMS and SGI Rackable C2112-4GP3/C1102-GP8 (Reedbush-U/H/L) in the Information Technology Center, The University of Tokyo.

References

- [1] J. Mao, Z. Liu, J. Zhou, H. Zhu, Q. Zhang, G. Chen, Z. Ren, *Adv. Phys.* **2018**, 67, 69.
- [2] T. Mori, *Small* **2017**, 13, 1702013.
- [3] N. Nandihalli, C.-J. Liu, T. Mori, *Nano Energy* **2020**, 78, 105186.
- [4] R. Vaßen, M. O. Jarligo, T. Steinke, D. E. Mack, D. Stöver, *Surf. Coatings Technol.* **2010**, 205, 938.
- [5] D. M. Smith, A. Maskara, U. Boes, *J. Non. Cryst. Solids* **1998**, 225, 254.
- [6] L. Hu, T. Zhu, X. Liu, X. Zhao, *Adv. Funct. Mater.* **2014**, 24, 5211.
- [7] Y. Cao, X. Su, F. Meng, T. P. Bailey, J. Zhao, H. Xie, J. He, C. Uher, X. Tang, *Adv. Funct. Mater.* **2020**, 30, 2005861.
- [8] B. Poudel, Q. Hao, Y. Ma, Y. Lan, A. Minnich, B. Yu, X. Yan, D. Wang, A. Muto, D. Vashaee, X. Chen, J. Liu, M. S. Dresselhaus, G. Chen, Z. Ren, *Science (80-.)*. **2008**, 320, 634.
- [9] S. H. Lo, J. He, K. Biswas, M. G. Kanatzidis, V. P. Dravid, *Adv. Funct. Mater.* **2012**, 22, 5175.
- [10] K. Biswas, J. He, I. D. Blum, C.-I. Wu, T. P. Hogan, D. N. Seidman, V. P. Dravid, M. G. Kanatzidis, *Nature* **2012**, 489, 414.
- [11] N. Sato, H. Ouchi, Y. Takagiwa, K. Kimura, *Chem. Mater.* **2016**, 28, 529.
- [12] Y. Iwasaki, K. Kitahara, K. Kimura, *Phys. Rev. Mater.* **2019**, 3, 061601.
- [13] Y. Miyazaki, D. Igarashi, K. Hayashi, T. Kajitani, K. Yubuta, *Phys. Rev. B* **2008**, 78, 214104.
- [14] Y. Miyazaki, H. Hamada, H. Nagai, K. Hayashi, *Materials (Basel)*. **2018**, 11, 926.
- [15] T. Takeuchi, *Zeitschrift für Krist. - Cryst. Mater.* **2009**, 224, 35.
- [16] K. Tobita, N. Sato, K. Kitahara, Y. Takagiwa, K. Kimura, *Mater. Trans.* **2016**, 57, 1045.
- [17] W. Li, J. Carrete, G. K. H. Madsen, N. Mingo, *Phys. Rev. B* **2016**, 93, 205203.

- [18] G. A. Slack, In *Semiconductors and Semimetals* (Eds.: Seitz, F.; Turnbull, D.; Ehrenreich, H.), Academic Press, New York, **1979**, p. 1.
- [19] T. Mori, *J. Solid State Chem.* **2019**, 275, 70.
- [20] Y. Kakefuda, K. Yubuta, T. Shishido, A. Yoshikawa, S. Okada, H. Ogino, N. Kawamoto, T. Baba, T. Mori, *APL Mater.* **2017**, 5, 126103.
- [21] S. Lee, K. Esfarjani, T. Luo, J. Zhou, Z. Tian, G. Chen, *Nat. Commun.* **2014**, 5, 3525.
- [22] S. Maier, S. Ohno, G. Yu, S. D. Kang, T. C. Chasapis, V. A. Ha, S. A. Miller, D. Berthebaud, M. G. Kanatzidis, G.-M. Rignanes, G. Hautier, G. J. Snyder, F. Gascoin, *Chem. Mater.* **2018**, 30, 174.
- [23] W. Zhang, N. Sato, K. Tobita, K. Kimura, T. Mori, *Chem. Mater.* **2020**, 32, 5335.
- [24] M. D. Nielsen, V. Ozolins, J. P. Heremans, *Energy Environ. Sci.* **2013**, 6, 570.
- [25] Y. Dong, A. R. Khabibullin, K. Wei, J. R. Salvador, G. S. Nolas, L. M. Woods, *ChemPhysChem* **2015**, 16, 3264.
- [26] M. Dutta, K. Pal, U. V. Waghmare, K. Biswas, *Chem. Sci.* **2019**, 10, 4905.
- [27] K. Pal, J. He, C. Wolverton, *Chem. Mater.* **2018**, 30, 7760.
- [28] M. Dutta, M. Samanta, T. Ghosh, D. J. Voneshen, K. Biswas, *Angew. Chemie Int. Ed.* **2021**, 60, 4259.
- [29] P. Acharyya, T. Ghosh, K. Pal, K. Kundu, K. Singh Rana, J. Pandey, A. Soni, U. V. Waghmare, K. Biswas, *J. Am. Chem. Soc.* **2020**, 142, 15595.
- [30] M. K. Jana, K. Pal, U. V. Waghmare, K. Biswas, *Angew. Chemie Int. Ed.* **2016**, 55, 7792.
- [31] B. Du, K. Chen, H. Yan, M. J. Reece, *Scr. Mater.* **2016**, 111, 49.
- [32] G. S. Nolas, D. T. Morelli, T. M. Tritt, *Annu. Rev. Mater. Sci.* **1999**, 29, 89.
- [33] Y. Zhu, Z. Han, F. Jiang, E. Dong, B.-P. Zhang, W. Zhang, W. Liu, *Mater. Today Phys.* **2021**, 16, 100327.

- [34] S. O. Long, A. V. Powell, S. Hull, F. Orlandi, C. C. Tang, A. R. Supka, M. Fornari, P. Vaqueiro, *Adv. Funct. Mater.* **2020**, *30*, 1909409.
- [35] Z. Liu, N. Sato, W. Gao, K. Yubuta, N. Kawamoto, M. Mitome, K. Kurashima, Y. Owada, K. Nagase, C.-H. Lee, J. Yi, K. Tsuchiya, T. Mori, *Joule* **2021**, *5*, 1196.
- [36] T. Takabatake, K. Suekuni, T. Nakayama, E. Kaneshita, *Rev. Mod. Phys.* **2014**, *86*, 669.
- [37] K. Suekuni, C. H. Lee, H. I. Tanaka, E. Nishibori, A. Nakamura, H. Kasai, H. Mori, H. Usui, M. Ochi, T. Hasegawa, M. Nakamura, S. Ohira-Kawamura, T. Kikuchi, K. Kaneko, H. Nishiate, K. Hashikuni, Y. Kosaka, K. Kuroki, T. Takabatake, *Adv. Mater.* **2018**, *30*, 1706230.
- [38] M. K. Jana, K. Pal, A. Warankar, P. Mandal, U. V. Waghmare, K. Biswas, *J. Am. Chem. Soc.* **2017**, *139*, 4350.
- [39] M. Dutta, S. Matteppanavar, M. V. D. Prasad, J. Pandey, A. Warankar, P. Mandal, A. Soni, U. V. Waghmare, K. Biswas, *J. Am. Chem. Soc.* **2019**, *141*, 20293.
- [40] K. Pal, Y. Xia, J. He, C. Wolverton, *Phys. Rev. Mater.* **2019**, *3*, 085402.
- [41] H. Lin, G. Tan, J.-N. Shen, S. Hao, L.-M. Wu, N. Calta, C. Malliakas, S. Wang, C. Uher, C. Wolverton, M. G. Kanatzidis, *Angew. Chemie Int. Ed.* **2016**, *55*, 11431.
- [42] K. Pal, Y. Xia, J. He, C. Wolverton, *Chem. Mater.* **2019**, *31*, 8734.
- [43] H. Liu, X. Shi, F. Xu, L. Zhang, W. Zhang, L. Chen, Q. Li, C. Uher, T. Day, G. J. Snyder, *Nat. Mater.* **2012**, *11*, 422.
- [44] L. Li, Y. Liu, J. Dai, A. Hong, M. Zeng, Z. Yan, J. Xu, D. Zhang, D. Shan, S. Liu, Z. Ren, J.-M. Liu, *J. Mater. Chem. C* **2016**, *4*, 5806.
- [45] S. Roychowdhury, M. K. Jana, J. Pan, S. N. Guin, D. Sanyal, U. V. Waghmare, K. Biswas, *Angew. Chemie Int. Ed.* **2018**, *57*, 4043.

- [46] J. Ding, J. L. Niedziela, D. Bansal, J. Wang, X. He, A. F. May, G. Ehlers, D. L. Abernathy, A. Said, A. Alatas, Y. Ren, G. Arya, O. Delaire, *Proc. Natl. Acad. Sci.* **2020**, *117*, 3930.
- [47] Y. He, T. Day, T. Zhang, H. Liu, X. Shi, L. Chen, G. J. Snyder, *Adv. Mater.* **2014**, *26*, 3974.
- [48] T. Mori, J. Martin, G. Nolas, *J. Appl. Phys.* **2007**, *102*, 073510.
- [49] Z. Liu, W. Zhang, W. Gao, T. Mori, *Energy Environ. Sci.* **2021**, Advance Article.
- [50] Y. Luo, J. Wang, Y. Li, J. Wang, *Sci. Rep.* **2016**, *6*, 29801.
- [51] X. Yu, H. Shao, X. Wang, Y. Zhu, D. Fang, J. Hong, **2019**.
- [52] T. Pandey, A. S. Nissimagoudar, A. Mishra, A. K. Singh, *J. Mater. Chem. A* **2020**, *8*, 13812.
- [53] Y. Shen, F. Q. Wang, Q. Wang, *Nano Energy* **2020**, *73*, 104822.
- [54] Y. Takagiwa, K. Kimura, *Sci. Technol. Adv. Mater.* **2014**, *15*, 044802.
- [55] Y. Yu, M. Cagnoni, O. Cojocaru-Mirédin, M. Wuttig, *Adv. Funct. Mater.* **2020**, *30*, 1904862.
- [56] X. Su, N. Zhao, S. Hao, C. C. Stoumpos, M. Liu, H. Chen, H. Xie, Q. Zhang, C. Wolverton, X. Tang, M. G. Kanatzidis, *Adv. Funct. Mater.* **2019**, *29*, 1806534.
- [57] H. Kageyama, K. Hayashi, K. Maeda, J. P. Attfield, Z. Hiroi, J. M. Rondinelli, K. R. Poeppelmeier, *Nat. Commun.* **2018**, *9*, 772.
- [58] Y. Pei, X. Shi, A. Lalonde, H. Wang, L. Chen, G. J. Snyder, *Nature* **2011**, *473*, 66.
- [59] Y. Pei, H. Wang, G. J. Snyder, *Adv. Mater.* **2012**, *24*, 6125.
- [60] W. Liu, K. C. Lukas, K. McEnaney, S. Lee, Q. Zhang, C. P. Opeil, G. Chen, Z. Ren, *Energy Environ. Sci.* **2013**, *6*, 552.
- [61] L.-D. Zhao, J. He, D. Berardan, Y. Lin, J.-F. Li, C. Nan, N. Dragoe, *Energy Environ. Sci.* **2014**, *7*, 2900.

- [62] G.-K. Ren, S. Wang, Z. Zhou, X. Li, J. Yang, W. Zhang, Y.-H. Lin, J. Yang, C.-W. Nan, *Nat. Commun.* **2019**, *10*, 2814.
- [63] J. Ding, B. Xu, Y. Lin, C. Nan, W. Liu, *New J. Phys.* **2015**, *17*, 083012.
- [64] C. Doussier, P. Léone, Y. Moëlo, *Solid State Sci.* **2004**, *6*, 1387.
- [65] C. Doussier, G. André, P. Léone, E. Janod, Y. Moëlo, *J. Solid State Chem.* **2006**, *179*, 486.
- [66] C. Doussier, Y. Moelo, P. Leone, *Synthesis and crystal structures of four new bromo-chalcogenides: MnSbS₂Br, MnBiSe₂Br and two allotropic forms of MnSbSe₂Br. Crystal chemistry of the MnPnQ₂XMnPnQ₂X family (Pn=SbPn=Sb, Bi; Q=SQ=S, Se; X=ClX=Cl, Br, I)*, Vol. 8, **2006**, pp. 652–659.
- [67] K. Momma, F. Izumi, *J. Appl. Crystallogr.* **2011**, *44*, 1272.
- [68] S. A. Sunshine, J. A. Ibers, *Acta Crystallogr. Sect. C Cryst. Struct. Commun.* **1987**, *43*, 1019.
- [69] T. Tadano, S. Tsuneyuki, *Phys. Rev. B* **2015**, *92*, 054301.
- [70] M. Simoncelli, N. Marzari, F. Mauri, *Nat. Phys.* **2019**, *15*, 809.
- [71] W. Zhou, Y. Cheng, K. Chen, G. Xie, T. Wang, G. Zhang, *Adv. Funct. Mater.* **2020**, *30*, 1903829.
- [72] B. Koley, A. Lakshan, P. R. Raghuvanshi, C. Singh, A. Bhattacharya, P. P. Jana, *Angew. Chemie Int. Ed.* **2021**, *60*, 9106.
- [73] C. Yuan, J. Li, L. Lindsay, D. Cherns, J. W. Pomeroy, S. Liu, J. H. Edgar, M. Kuball, *Commun. Phys.* **2019**, *2*, 43.
- [74] R. Wei, S. Song, K. Yang, Y. Cui, Y. Peng, X. Chen, X. Hu, X. Xu, *J. Appl. Phys.* **2013**, *113*, 053503.
- [75] H. R. Shanks, P. D. Maycock, P. H. Sidles, G. C. Danielson, *Phys. Rev.* **1963**, *130*, 1743.

- [76] A. Jeżowski, B. A. Danilchenko, M. Boćkowski, I. Grzegory, S. Krukowski, T. Suski, T. Paszkiewicz, *Solid State Commun.* **2003**, *128*, 69.
- [77] H. Y. Chen, N. Savvides, T. Dasgupta, C. Stiewe, E. Mueller, *Phys. status solidi* **2010**, *207*, 2523.
- [78] D. T. Morelli, T. Caillat, J.-P. Fleurial, A. Borshchevsky, J. Vandersande, B. Chen, C. Uher, *Phys. Rev. B* **1995**, *51*, 9622.
- [79] C. B. Satterthwaite, R. W. Ure, *Phys. Rev.* **1957**, *108*, 1164.
- [80] Z. Tian, J. Garg, K. Esfarjani, T. Shiga, J. Shiomi, G. Chen, *Phys. Rev. B* **2012**, *85*, 184303.
- [81] E. S. Toberer, A. F. May, G. J. Snyder, *Chem. Mater.* **2010**, *22*, 624.
- [82] T. Caillat, J.-P. Fleurial, A. Borshchevsky, *J. Phys. Chem. Solids* **1997**, *58*, 1119.
- [83] L.-D. Zhao, S.-H. Lo, Y. Zhang, H. Sun, G. Tan, C. Uher, C. Wolverton, V. P. Dravid, M. G. Kanatzidis, *Nature* **2014**, *508*, 373.
- [84] K. Takahata, Y. Iguchi, D. Tanaka, T. Itoh, I. Terasaki, *Phys. Rev. B* **2000**, *61*, 12551.
- [85] P. Giannozzi, S. Baroni, N. Bonini, M. Calandra, R. Car, C. Cavazzoni, D. Ceresoli, G. L. Chiarotti, M. Cococcioni, I. Dabo, A. Dal Corso, S. de Gironcoli, S. Fabris, G. Fratesi, R. Gebauer, U. Gerstmann, C. Gougoussis, A. Kokalj, M. Lazzeri, L. Martin-Samos, N. Marzari, F. Mauri, R. Mazzarello, S. Paolini, A. Pasquarello, L. Paulatto, C. Sbraccia, S. Scandolo, G. Sclauzero, A. P. Seitsonen, A. Smogunov, P. Umari, R. M. Wentzcovitch, *J. Phys. Condens. Matter* **2009**, *21*, 395502.
- [86] P. Giannozzi, O. Andreussi, T. Brumme, O. Bunau, M. Buongiorno Nardelli, M. Calandra, R. Car, C. Cavazzoni, D. Ceresoli, M. Cococcioni, N. Colonna, I. Carnimeo, A. Dal Corso, S. de Gironcoli, P. Delugas, R. A. DiStasio, A. Ferretti, A. Floris, G. Fratesi, G. Fugallo, R. Gebauer, U. Gerstmann, F. Giustino, T. Gorni, J. Jia, M. Kawamura, H.-Y. Ko, A. Kokalj, E. Küçükbenli, M. Lazzeri, M. Marsili, N. Marzari, F. Mauri, N. L. Nguyen, H.-V. Nguyen, A. Otero-de-la-Roza, L. Paulatto, S. Poncé, D. Rocca, R. Sabatini, B. Santra, M.

Schlipf, A. P. Seitsonen, A. Smogunov, I. Timrov, T. Thonhauser, P. Umari, N. Vast, X. Wu, S. Baroni, *J. Phys. Condens. Matter* **2017**, 29, 465901.

[87] P. E. Blöchl, *Phys. Rev. B* **1994**, 50, 17953.

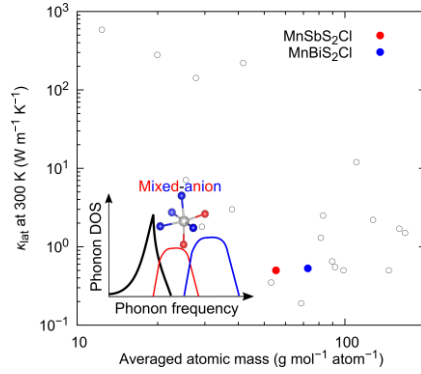
[88] G. Kresse, D. Joubert, *Phys. Rev. B* **1999**, 59, 1758.

[89] G. I. Csonka, J. P. Perdew, A. Ruzsinszky, P. H. T. Philipsen, S. Lebègue, J. Paier, O. A. Vydrov, J. G. Ángyán, *Phys. Rev. B* **2009**, 79, 155107.

[90] T. Tadano, Y. Gohda, S. Tsuneyuki, *J. Phys. Condens. Matter* **2014**, 26, 225402.

Naoki Sato,* Norihide Kuroda, Shun Nakamura, Yukari Katsura, Ikuzo Kanazawa, Kaoru Kimura, and Takao Mori

Bonding Heterogeneity in Mixed-Anion Compounds Realizes Ultralow Lattice Thermal Conductivity



Bonding heterogeneity in chalcogenides MnPnS_2Cl ($\text{Pn} = \text{Sb}, \text{Bi}$) derives a peak splitting of the phonon density of states, which induces a large amount of scattering phase space. Consequently, MnPnS_2Cl exhibits ultralow lattice thermal conductivity κ_{lat} despite their relatively low averaged atomic mass. Our findings will encourage the exploration of novel mixed-anion materials with lightweight and low κ_{lat} .